JMEPEG (2012) 21:1091–1098
DOI: 10.1007/s11665-011-9983-3

1059-9495/$19.00

The Kinetics of Phase Transformations During Tempering in Laser Melted High Chromium Cast Steel

M.Y. Li, Y. Wang, and B. Han

(Submitted June 1, 2010; in revised form February 19, 2011)

The precipitation of secondary carbides in the laser melted high chromium cast steels during tempering at 300-650 °C for 2 h in air furnace was characterized and the present phases was identified, by using transmission electron microscopy. Laser melted high chromium cast steel consists of austenitic dendrites and interdendritic $M_{23}C_6$ carbides. The austenite has such a strong tempering stability that it remains unchanged at temperature below 400 °C and the secondary hardening phenomenon starts from 450 °C to the maximum value of 672 HV at 560 °C. After tempering at 450 °C fine $M_{23}C_6$ carbides precipitate from the supersaturated austenite preferentially. In addition, the dislocation lines and slip bands still exist inside the austenite. While tempering at temperature below 560 °C, the secondary hardening simultaneously results from the martensite phase transformation and the precipitation of carbides as well as dislocation strengthening within a refined microstructure. Moreover, the formation of the ferrite matrix and large quality of coarse lamellar M_3C carbides when the samples were tempered at 650 °C contributes to the decrease of hardness.

Keywords hardness, high chromium cast steel, laser surface melting, secondary carbides, tempering characteristic

1. Introduction

Laser surface melting (LSM) is a very promising technique to improve properties of materials, such as wear resistance and ductility (Ref 1-3). It involves rapid heating with melting followed by a quenching to modify the near surface microstructure without changing its chemical compositions. The typical heating/cooling rates and thermal gradients associated with LSM are 10^4-10^8 K/s and 10^5-10^8 K/m, respectively (Ref 4, 5). As a result, LSM often produces metastable microstructures with novel properties.

High chromium cast steels are used for hot rollers since they possess a high wear resistance at the working temperature. However, the high alloy content in high chromium cast steels inherently gives rise to carbide segregation at grain boundaries and a coarse-grained microstructure by centrifugal casting. LSM of high chromium cast steels allows for the complete dissolution of large brittle carbides, leading to homogeneous and extremely fine microstructures (Ref 6). In addition, laser melted layers undergo a nonequilibrium metallurgical process, while the traditional transformations are often inhibited and a large amount of austenite appears.

Since retained austenite is stabilized if cooling is interrupted before completion of the martensitic transformation, tempering is very effective in eliminating retained austenite in the laser melted steels (Ref 7). Owing to their large interface area and high free energy, the fine nonequilibrium microstructures will exhibit a spontaneous trend to evolve into coarse equilibrium ones in agreement with thermodynamical principles through recovery and recrystallization when reheated below the equilibrium transformation temperature. It was reported (Ref 8-10) that the evolution will manifestly slow down if precipitation occurred simultaneously. This indicates that the free energy of the system is not a unique factor for determining the evolution rate of the microstructures, and is not even the dominant one in some cases. The history of the thermo-mechanical process, including the part that takes place before $\gamma \rightarrow \alpha$ transformation, will probably affect the thermostability of transformation products. Studies of the effect of heat treatment on microstructure of the laser melted steels are scarce, but they have shown that secondary hardening could be achieved, more importantly, that the hardness and the secondary hardening temperature are higher than after conventional quenching and tempering treatments (Ref 11, 12). Therefore, further studies of the hardening behavior of the laser melted high chromium cast steels are necessary before practical applications.

In this study, we give a detailed investigation of the phase transformations during tempering of laser melted high chromium cast steel, aiming to achieve a better understanding of the tempering behavior of the laser melted steels.

2. Experimental Procedure

The chemical composition of the as-received high chromium cast steel is listed in Table 1. In consideration of self-quenching, specimens used in the experiment were manufactured in the size of 200 × 150 × 60 mm. LSM was performed using a continuous wave CO_2 laser, with argon as shielding gas to minimize oxidation, and the following parameters: power 2.7 kW, scanning speed 300 mm/min, beam diameter 3 mm.

M.Y. Li, Y. Wang, and **B. Han**, College of Electromechanical Engineering, China University of Petroleum, Dongying 257061, China. Contact e-mail: lmy_102411@163.com.

After laser treatment, the specimens were tempered at temperatures of 300-650 °C for 2 h in air furnace.

For metallographic examination, the crosssections of the laser melted specimens were polished and then etched in 4% nital and chloroazotic acid, respectively. The microstructure of the laser melted layer was analyzed by scanning electron microscopy (SEM) and transmission electron microscopy (TEM). The phases present in the laser melted layer tempered at different temperatures were identified by x-ray diffraction (XRD). Vickers hardness measurements were carried out on MH-3 equipment using a load of 200 g.

3. Results and Discussion

3.1 Microstructure in the Melted Layer

The microstructure of high chromium cast steel by LSM is shown in Fig. 1. As it can be seen, large brittle carbides were dissolved completely and dense ultrafine austenitic dendrites were formed in the melted layer (Fig. 1a). Ultrafine granular carbides at the grain boundaries can be seen at high magnification in Fig. 1(b), which are revealed to be $M_{23}C_6$ carbides (Ref 6). The austenite is strengthened by solid solution, dislocations and ultrafine grains, which are likely to contribute to the relatively high hardness compared with the conventional austenite.

Table 1 Chemical composition of the as-received high chromium steel (wt.%)

C	Cr	Ni	Mo	V	Mn	P	S
1.09	10.48	0.56	1.04	0.39	0.53	0.031	0.017

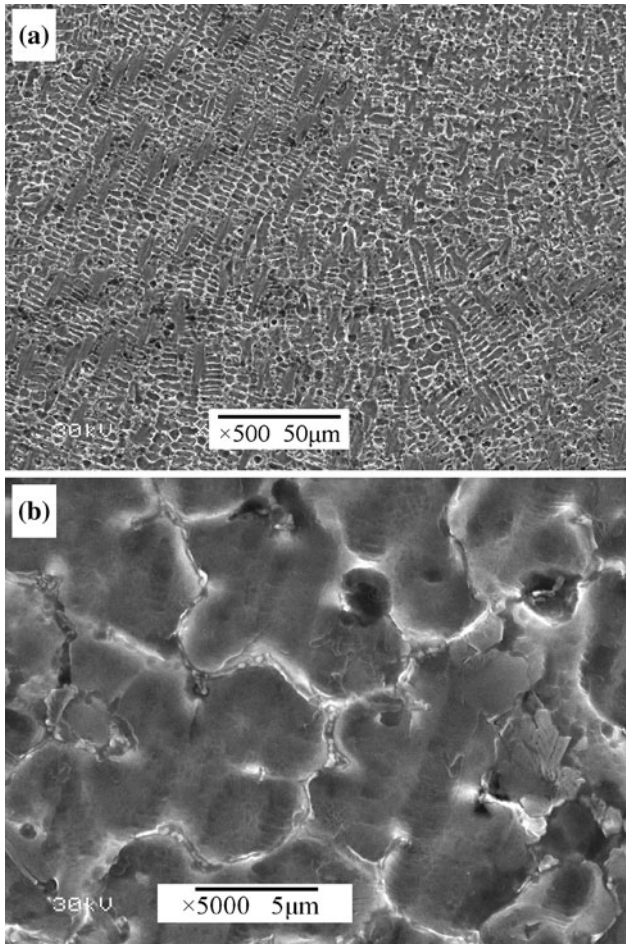

Fig. 1 Microstructure of the laser melted steel (a) at low magnification and (b) at high magnification

3.2 Hardness of the Laser Melted Layer After Tempering

Hardness curves of the laser melted layers tempered at different temperatures are shown in Fig. 2. As it is can be seen, with the increase of tempering temperature, the hardness remains constant or only slightly decreases below 400 °C, indicating the high tempering stability of the austenite. The secondary hardening appears, beginning at 450 °C, and reaching a maximum value of 672 HV at 560 °C. When the tempering temperature exceeds 600 °C, the hardness of the laser melted layer decreases quickly.

Besides the supersaturation of both carbon and alloy elements, the austenite has a high density of dislocation (Ref 6). Usually, the crystal defects supply favorable nucleation

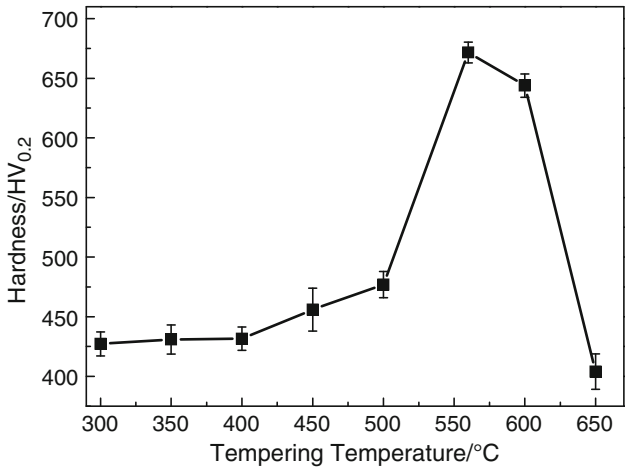

Fig. 2 Hardness of the laser melted layer vs. tempering temperature

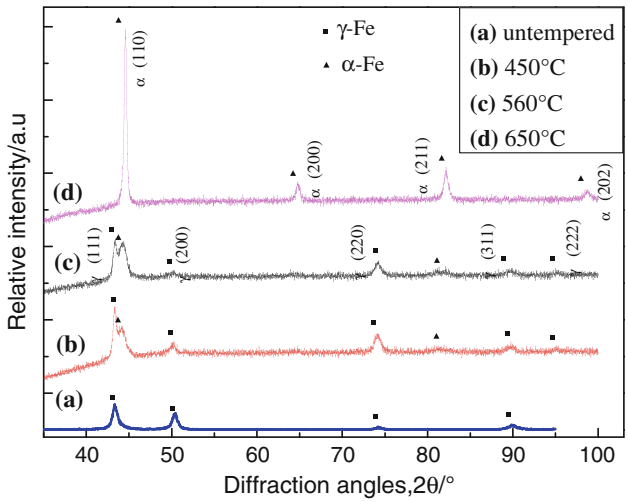

Fig. 3 X-ray patterns of the laser melted layer at different temperatures

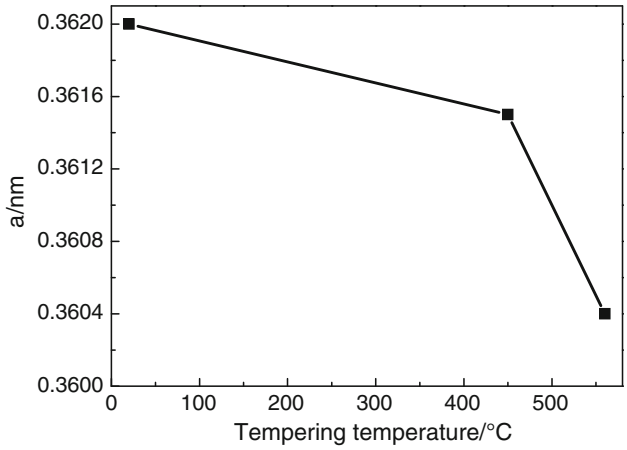

Fig. 4 The lattice parameters of austenite in the melted layer tempered at different temperatures

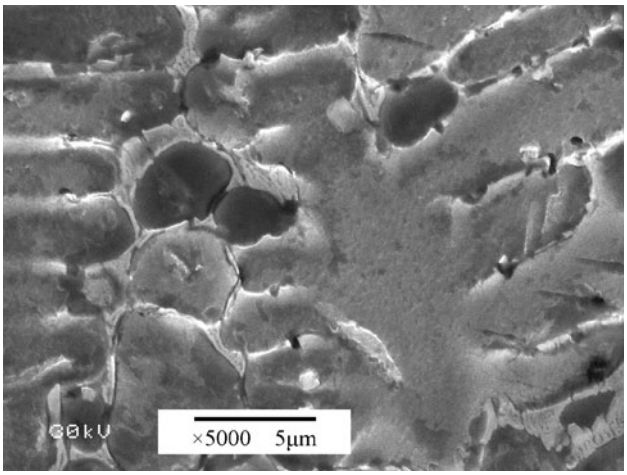

Fig. 5 Microstructure of the laser melted layer tempered at 450 °C

sites for precipitation of these elements in the form of carbides. Moreover, the driving force of the precipitation is increased (Ref 13). However, the austenite has a high tempering stability, as shown in Fig. 2, while the following reasons can be speculated. (1) The alloying elements preclude solid state transformation of the austenite and inhibit the precipitation and growth of carbides (Ref 14). (2) The alloying elements in the austenite change the size of the interstices of the grains and promote the diffusive activation energy of atoms (Ref 15).

3.3 XRD Analysis of the Laser Melted Layer Subjected to Tempering

The x-ray diffractogram of the laser melted layer shows peaks corresponding to austenite (Fig. 3a). Tempering at 450 °C leads to a decrease of the relative intensity of γ-Fe peaks and the appearance of small amplitude peaks of α-Fe (Fig. 3b). The amplitude of the α-Fe peaks increases with the increased tempering temperature and the peaks of retained austenite almost completely disappear after tempering at 650 °C (Fig. 3d).

According to the x-ray diffractograms in Fig. 3, the lattice parameters of austenite in the melted layer after tempering at different temperatures can be calculated. As shown in Fig. 4,

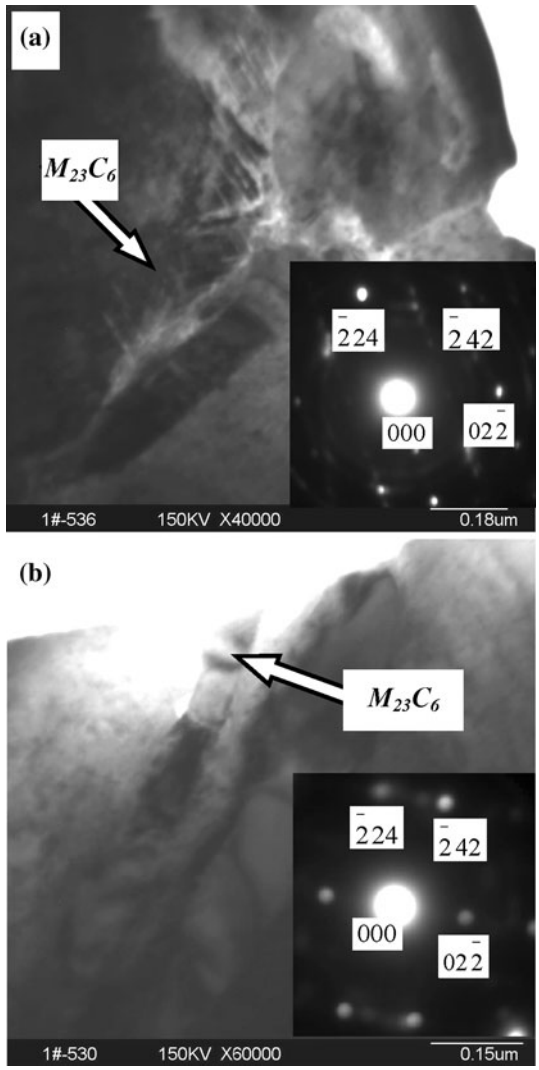

Fig. 6 TEM micrographs of the laser melted layer tempered at 450 °C (a) stripy $M_{23}C_6$ carbides at the grain boundaries and (b) rod-like shaped $M_{23}C_6$ carbides inside the austenite

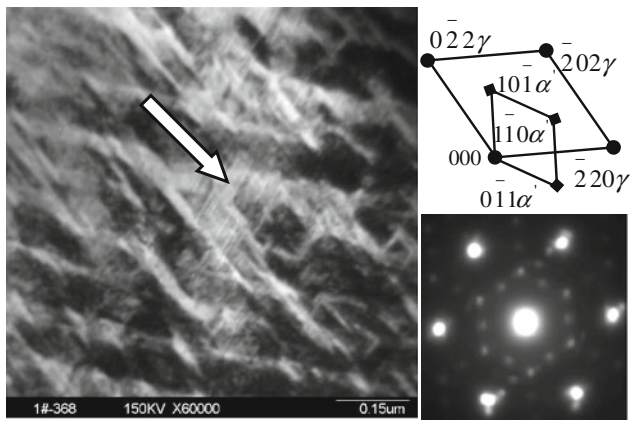

Fig. 7 Martensite inside the dendrites of the laser melted layer tempered at 450 °C

the mean lattice parameters of the FCC austenite phase in the laser melted layer amounts to 0.36206 nm. Comparison of the experimentally determined *d* spacings with those given in

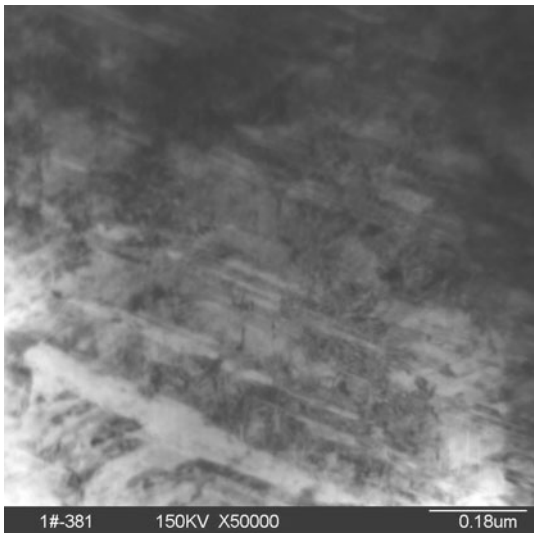

Fig. 8 Dislocation lines and slip bands inside the austenite

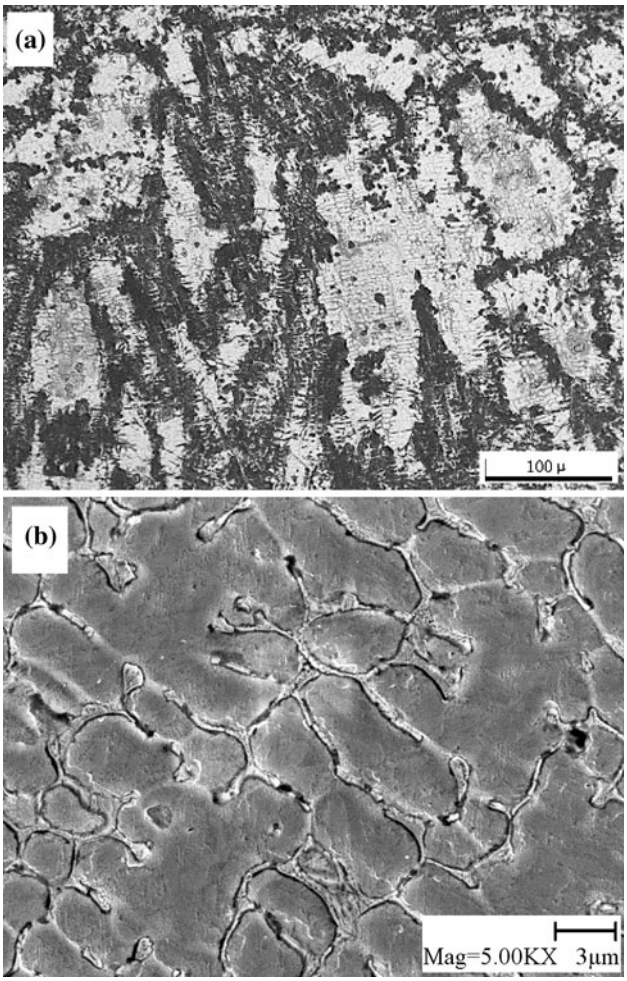

Fig. 9 (a) Optical micrograph of laser melted layer tempered at 560 °C and (b) carbides morphology

the standard x-ray powder diffraction data indicates that the lattice parameters of austenite in the melted layer are greater than the normal lattice constant of austenite (0.3585 nm) (Ref 16).

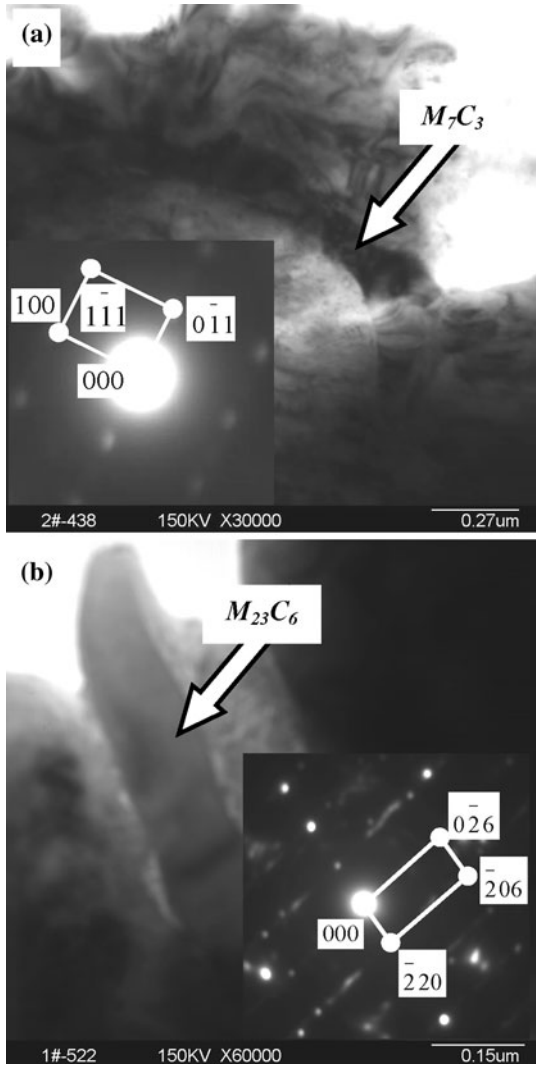

Fig. 10 Stripy carbides at the grain boundary (a) M_7C_3 carbides and (b) $M_{23}C_6$ carbides

The increase of the lattice parameter suggests that a significant dissolution of alloying elements, such as C, Cr, Mo, V, commenced in the austenite. In addition, with the increase of tempering temperature, the mean lattice parameter of austenite decreases.

3.4 Tempering at 450 °C

According to XRD in Fig. 3, the laser melted layer appears to be a mixed martensite-austenite structure after tempering at 450 °C for 2 h. As it can be seen in Fig. 5, a few fine precipitates appear, while no carbide peaks are found in XRD patterns because the amount of carbides is insufficient to be detected by this technique. According to the TEM morphology, $M_{23}C_6$ carbides have precipitated both on the austenitic dendrite boundaries with stripy shape (Fig. 6a) and within the austenite with rod-like shape (Fig. 6b). The TEM observation reveals lamellar martensite within the austenitic dendrites, as shown in Fig. 7. In addition, the dislocation lines and slip bands still exist inside the austenite (Fig. 8).

Laser irradiation leads to the complete dissolution of M_7C_3 carbides, and during the subsequent cooling, the increase in the carbon and alloying elements concentrate in the solid solution,

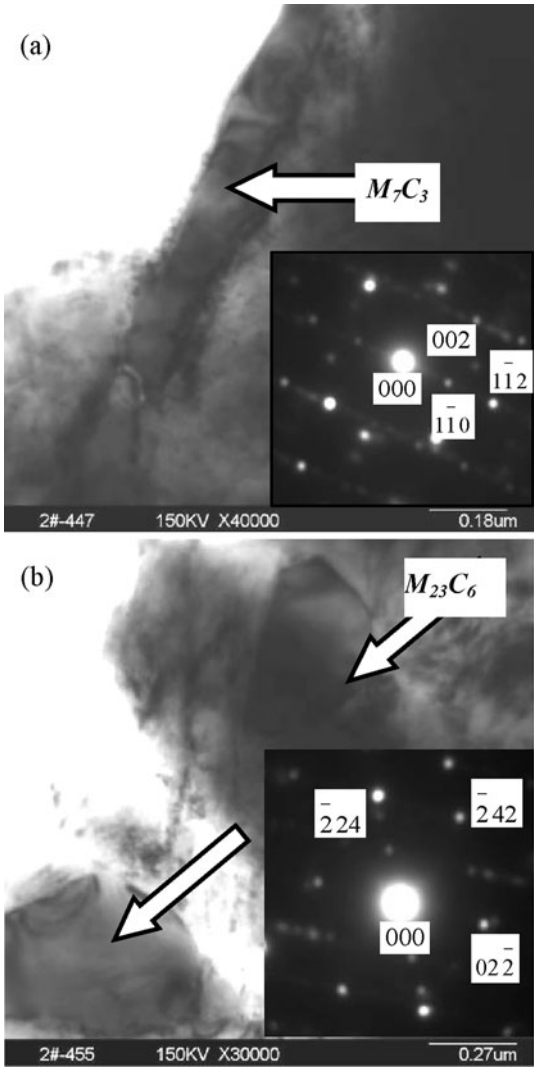

Fig. 11 Carbides inside the dendrites (a) fine rod-like shaped M_7C_3 carbides and (b) granular $M_{23}C_6$ carbides

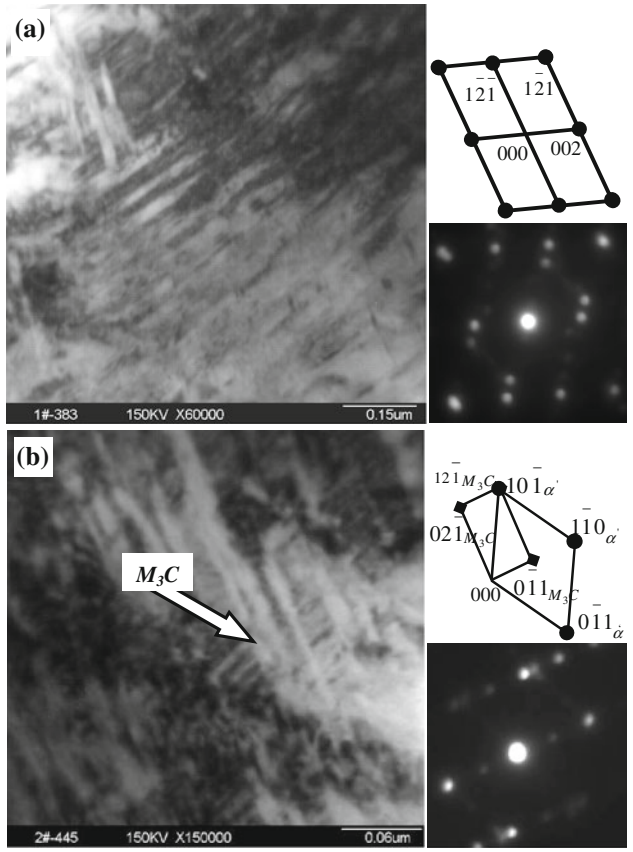

Fig. 12 (a) Martensite in the laser melted layer tempered at 560 °C and (b) lamellar M_3C carbides inside martensite

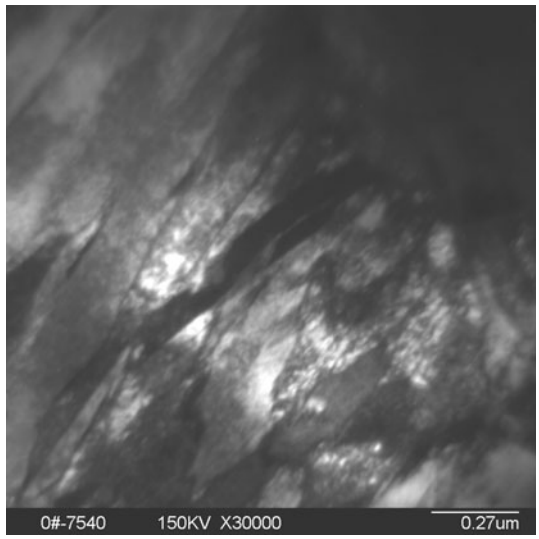

Fig. 13 High-density dislocations inside the austenite

which raises the ranges of these transformations toward high temperatures. The phase evolution in the laser melted steels is one of involving a dynamical interplay between nucleation, growth and coarsening of various metastable and stable phases. When tempering at 450 °C, the diffusion coefficients of alloying elements in austenite are low (Ref 11), thus the preferential precipitation of $M_{23}C_6$ carbides rather than M_7C_3 carbides is explained in terms of the good lattice matching between austenite and $M_{23}C_6$ carbides, decreasing the free surface energy and nucleation activation energy (Ref 15, 17). This study shows that the destabilization of austenite occurred after the precipitation of secondary carbide $M_{23}C_6$ within the phase, by depleting carbon and chromium contents of matrix, which decreased the lattice parameters of the austenite (Fig. 4) and increased the M_s temperature of the austenitic matrix. This caused austenite transform to martensite during subsequently cooling to ambient temperature (Fig. 7). Also, the tempering of the laser melted layer, causing a residual stress relief of the material, may also contribute to destabilizing austenite (Ref 18) so that the austenite content in the matrix decreased. As a result, fine $M_{23}C_6$ carbides precipitated from austenite preferentially and a small amount of martensite formed as well as high density of dislocations result in the increase of the hardness slightly.

3.5 Tempering at 560 °C

As shown in Fig. 9(a), structural characteristics of the laser melted layer after tempering at 560 °C change dramatically compared with those shown in Fig. 1(a). Moreover, it could be

noted that fine lamellar carbides are precipitated at the grain boundaries with the thickness of approximately 200-500 nm as shown in Fig. 9(b).

TEM examinations in Fig. 10 give more information on the secondary hardening carbides. These stripy carbides at the grain boundaries are determined to be M_7C_3 (Fig. 10a) and $M_{23}C_6$ carbides (Fig. 10b). Moreover, the fine rod-like shaped M_7C_3 carbides (Fig. 11a) and granular $M_{23}C_6$ carbides (Fig. 11b) coexist within the dendrites. During tempering at 560 °C, the diffusion coefficients of alloying elements in austenite are improved, thus the precipitation of the secondary carbides is controlled by the diffusion of alloying elements such as Cr, Mo, and V within the austenite. According to the phase diagram of Fe-C-Cr (Ref 3), the complex hexagonal M_7C_3 carbide will precipitate from the austenite preferentially, and then they partially dissolved followed by the precipitation of $M_{23}C_6$ carbides.

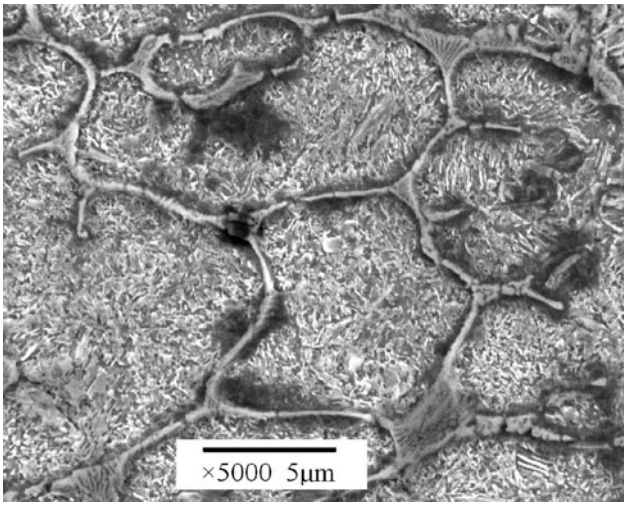

Fig. 14 SEM micrograph of the laser melted layer tempered at 650 °C

In addition, TEM observation reveals lamellar martensite within the dendrites, as shown in Fig. 12(a), while the morphology and distribution of M_3C carbides in the decomposed regions are illustrated in Fig. 12(b). As it is shown, M_3C carbides are distributed as some parallel rows, probably perpendicular to the lamellar martensite. In this particular case, the OR between M_3C carbides and martensite is deduced to be Bagaryatsky relationship: $(100)M_3C//(1\bar{1}0)\alpha'$. It is important to note that thin lamellar M_3C carbides perpendicular to the lamellar martensite are not the results of austenitic decomposition but those of martensite.

As illustrated in Fig. 13, high-density dislocations and stacking faults are observed within the retained austenite of laser melted layer after tempering at 560 °C. Recovery occurring during reheating caused the density of dislocations to decrease in some degree. However, the dislocations pinned by the precipitates were relatively stable (Ref 18, 19). Thus, the

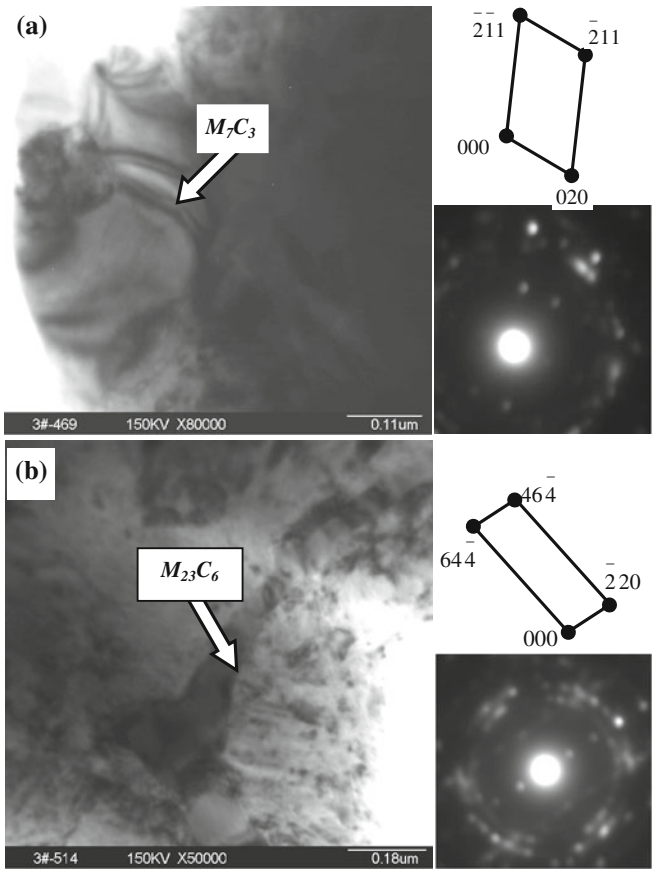

Fig. 15 (a) TEM micrograph of the laser melted layer tempered at 650 °C, (b) massive M_7C_3 carbide, and (c) stripy $M_{23}C_6$ carbide at the grain boundaries

dislocation networks in the austenitic matrix were not completely eliminated by tempering at 560 °C, contributing to the strength of the laser melted high chromium cast steel. As a result, the combined effects of the martensite phase transformation and the precipitation of carbides as well as dislocation strengthening within a refined microstructure result in the secondary hardening after tempering at 560 °C.

3.6 Tempering at 650 °C

When the tempering temperature was elevated to 650 °C, the size of the precipitates increased obviously and a continuous carbide network was located at the grain boundaries (Fig. 14). The precipitates at the grain boundaries are identified as massive M_7C_3 carbides (Fig. 15a) and stripy $M_{23}C_6$ carbides (Fig. 15b), while the skeleton-like M_7C_3 carbides (Fig. 16a) and stripy $M_{23}C_6$ carbides (Fig. 16b) are present inside the grain. It is possible that climbing of boundary dislocations brings about disappearance of dendritic boundaries and coalition of neighboring dendrites, where recrystallization will nucleate. Finally, the austenite recrystallizes and traditional transformation is restored. Thus, a pearlite structure with 60 nm cementite spacing is found in the sample tempered at 650 °C (Fig. 16c).

In a supersaturated solid solution, diffusion effects may bring about the formation of new phases. The types of the secondary carbide are determined by thermodynamic considerations, and the temperature is the key parameter influencing the concentration fluctuations which produce nuclei of the new phase. This is why different precipitates were found for different tempering temperatures. The coarsening processes that occur were caused by the diffusion controlled transfer of solute in the matrix. The growth of the M_3C carbides at 650 °C is expected to be controlled by carbon diffusion and is thus very rapid (Ref 20). With the precipitation of a large number of M_3C carbides, the carbon content in the matrix become lower than before, which lessens the solution strengthening effect. In addition, the coarse lamellar M_3C carbides have lower dispersion strengthening effect, and therefore the hardness decreased.

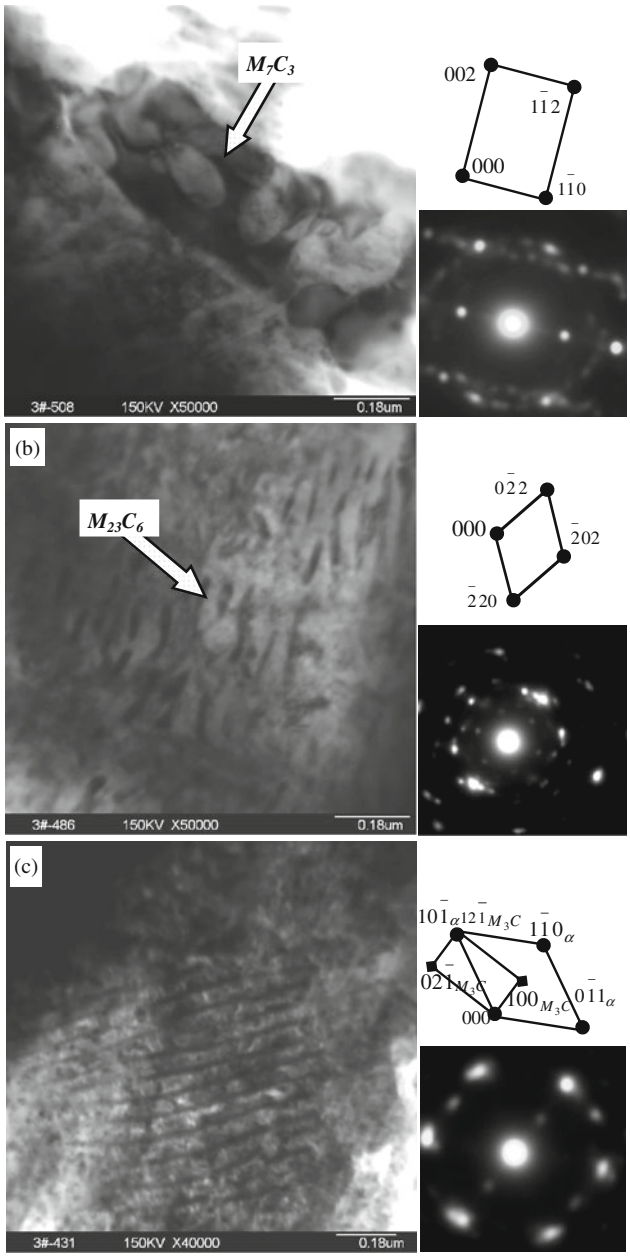

Fig. 16 Morphologies of carbides inside the dendrites after tempering at 650 °C (a) skeleton-like M_7C_3 carbides, (b) stripy $M_{23}C_6$ carbides, and (c) ferrite and lamellar M_3C carbides

4. Conclusions

(1) LSM of high chromium cast steel leads to the complete dissolution of brittle carbides, and the melted layer consists of austenitic dendrites and interdendritic $M_{23}C_6$ carbides particles. The structure of the austenite contains not only a large amount of supersaturated alloy elements, but also a high density of crystal defects.

(2) As far as the laser melted steel concerned, the austenite has such a strong tempering stability that it remains unchanged below 400 °C. The secondary hardening appears, beginning at 450 °C, and reaching a maximum at 560 °C. When the tempering temperature exceeds 600 °C, the hardness of the laser melted layer decreases quickly.

(3) After tempering at 450 °C fine $M_{23}C_6$ carbides precipitated from the supersaturated austenite preferentially. While tempering below 560 °C, the secondary hardening simultaneously results from the martensite phase transformation and the precipitation of carbides as well as dislocation strengthening within a refined microstructure. Moreover, the fall from peak hardness was accompanied by the formation of the ferrite matrix and large quality of coarse lamellar M_3C carbides after tempering at 650 °C.

Acknowledgments

The authors would like to acknowledge the supports from the Natural Science Foundation of Shandong Province (ZR2009FM030) and the Special Fund of Central University Fundamental Scientific Research Professional expenses (10CX04026A).

References

1. S. Kac and J. Kusinski, SEM and TEM Microstructural Investigation of High-Speed Tool Steel After Laser Melting, *Mater. Chem. Phys.*, 2003, **81**(2–3), p 510–512
2. R. Colaco, C. Pina, and R. Vilar, Influence of the Processing Conditions on the Abrasive Wear Behaviour of a Laser Surface Melted Tool Steel, *Scr. Mater.*, 1999, **41**(7), p 715–721
3. P.A. Molian and H.S. Rajasekhara, Analysis of Microstructures of Laser Surface-Melted Tool Steels, *J. Mater. Sci. Lett.*, 1986, **5**, p 1292–1294
4. Y.P. Lei, H. Murakawa, Y.W. Shi, and X.Y. Li, Numerical Analysis of the Competitive Influence of Marangoni Flow and Evaporation on Heat Surface Temperature and Molten Pool Shape in Laser Surface Remelting, *Comput. Mater. Sci.*, 2001, **21**, p 276–290
5. J.H. Abboud, K.Y. Benyounis, A.G. Olabi, and M.S.J. Hashmi, Laser Surface Treatments of Iron-Based Substrates for Automotive Application, *J. Mater. Process. Technol.*, 2007, **182**(1–3), p 427–431
6. M. Li, Y. Wang, B. Han, W. Zhao, and T. Han, Microstructure and Properties of High chromium cast steel Roller After Laser Surface Melting, *Appl. Surf. Sci.*, 2009, **255**, p 7575–7579
7. M. Wang, Y. Wang, and F. Sun, Tempering Behavior of a Semi-High Speed Steel Containing Nitrogen, *Mater. Sci. Eng. A*, 2006, **438–440**, p 1139–1142
8. H. Tanaka, M. Murata, F. Abe, and K. Yagi, The Effect of Carbide Distributions on Long-Term Creep Rupture Strength of SUS321H and SUS347H Stainless Steels, *Mater. Sci. Eng. A*, 1997, **234–236**, p 1049–1052
9. S.G. Hong, W.B. Lee, and C.G. Park, The Effects of Tungsten Addition on the Microstructural Stability of 9Cr-Mo Steels, *J. Nucl. Mater.*, 2001, **288**(2–3), p 202–207
10. H. Sakasegawa, T. Hirose, A. Kohyama, Y. Katoh, T. Harada, and K. Asakura, Microstructural Stability of Reduced Activation Ferritic/Martensitic Steels Under High Temperature and Stress Cycling, *Fusion Eng. Des.*, 2002, **61–62**, p 671–675
11. R. Colaco and R. Vilar, Effect of Laser Surface Melting on the Tempering Behaviour of DIN X42Cr13 Stainless Tool Steel, *Scr. Mater.*, 1997, **38**(1), p 107–113
12. R. Wu, C.-s. Xie, M. Hu, and W.-p. Cai, Laser-Melted Surface Layer of Steel X165CrMoV12-1 and Its Tempering Characteristics, *Mater. Sci. Eng. A*, 2000, **278**(1–2), p 1–4
13. H.M. Wang and H.W. Bergman, Annealing Laser-Melted Ductile Iron by Pulsed Nd:YAG Laser Radiation, *Mater. Sci. Eng. A*, 1995, **196**(1–2), p 171–176
14. G. Zajac and J. Pacyna, The Kinetics of Phase Transformations During Tempering in Structural Steels With Nickel, *J. Mater. Process. Technol.*, 2005, **162–163**, p 442–446
15. J. Wang, R.L. Zuo, Z.P. Sun, C. Li, H.H. Liu, H.S. Yang, B.L. Shen, and S.J. Huang, Influence of Secondary Carbides Precipitation and Transformation on Hardening Behavior of a 15Cr-1Mo-1.5V White Iron, *Mater. Charact.*, 2005, **55**(3), p 234–240
16. H.-h. Liu, J. Wang, B.-l. Shen, H.-s. Yang, S.-j. Gao, and S.-j. Huang, Effects of Deep Cryogenic Treatment on Property of 3Cr13Mo1V1.5 High Chromium Cast Iron, *Mater. Des.*, 2007, **28**(3), p 1059–1064
17. M. Radulovic, M. Fiset, K. Peev, and M. Tomovic, Influence of Vanadium on Fracture Toughness and Abrasion Resistance in High Chromium White Cast Irons, *J. Mater. Sci.*, 1994, **29**, p 5085–5094
18. Z.L. Xie, Y. Liu, and H. Hanninen, Stabilization of Retained Austenite Due to Partial Martensitic Transformations, *Acta Metall. Mater.*, 1994, **42**(12), p 4117–4133
19. H.B. Wu, H.T. Jiang, S.W. Yang, D. Tang, and X.L. He, Thermal Stability of Non-equilibrium Microstructure in Microalloyed Steel During Reheating, *Acta Metall. Sin. (English)*, 2007, **20**(5), p 313–326
20. Z.K. Liu and J. Agren, Morphology of Cementite Decomposition in an Fe-Cr-C alloy, *Metall. Mater. Trans. A Phys. Metall. Mater. Sci.*, 1991, **22**, p 1753–1759